Atmos. Meas. Tech., 8, 2699–2714, 2015
www.atmos-meas-tech.net/8/2699/2015/
doi:10.5194/amt-8-2699-2015

Atmospheric Measurement Techniques
Open Access

The effect of radiometer placement and view on inferred directional and hemispheric radiometric temperatures of an urban canopy

C. Adderley[1], **A. Christen**[1], **and J. A. Voogt**[2]

[1]Department of Geography/Atmospheric Science Program, The University of British Columbia, Vancouver, BC, Canada
[2]Department of Geography, Western University, London, ON, Canada

Correspondence to: A. Christen (andreas.christen@ubc.ca)

Received: 04 December 2014 – Published in Atmos. Meas. Tech. Discuss.: 18 February 2015
Revised: 02 June 2015 – Accepted: 05 June 2015 – Published: 03 July 2015

Abstract. Any radiometer at a fixed location has a biased view when observing a convoluted, three-dimensional surface such as an urban canopy. The goal of this contribution is to determine the bias of various sensors views observing a simple urban residential neighbourhood (nadir, oblique, hemispherical) over a 24 hour cycle under clear weather conditions. The error in measuring a longwave radiation flux density (L) and/or inferring surface temperatures (T_0) is quantified for different times over a diurnal cycle. Panoramic time-sequential thermography (PTST) data were recorded by a thermal camera on a hydraulic mast above a residential canyon in Vancouver, BC. The data set resolved sub-facet temperature variability of all representative urban facets in a 360° swath repetitively over a 24-hour cycle. This data set is used along with computer graphics and vision techniques to project measured fields of L for a given time and pixel onto texture sheets of a three-dimensional urban surface model at a resolution of centimetres. The resulting data set attributes L of each pixel on the texture sheets to different urban facets and associates facet location, azimuth, slope, material, and sky view factor. The texture sheets of L are used to calculate the complete surface temperature ($T_{0,\mathrm{C}}$) and to simulate the radiation in the field of view (FOV) of narrow and hemispheric radiometers observing the same urban surface (in absence of emissivity and atmospheric effects). The simulated directional ($T_{0,\mathrm{d}}$) and hemispheric ($T_{0,\mathrm{h}}$) radiometric temperatures inferred from various biased views are compared to $T_{0,\mathrm{C}}$. For a range of simulated off-nadir (ϕ) and azimuth (Ω) angles, $T_{0,\mathrm{d}}(\phi,\Omega)$ and $T_{0,\mathrm{C}}$ differ between -2.6 and +2.9 K over the course of the day. The effects of effective anisotropy are highest in the daytime, particularly around sunrise and sunset when different views can lead to differences in $T_{0,\mathrm{d}}(\phi,\Omega)$ that are as high as 3.5 K. For a sensor with a narrow FOV in the nadir of the urban surface, $T_{0,\mathrm{d}}(\phi=0)$ differs from $T_{0,\mathrm{C}}$ by +1.9 K (day) and by -1.6 K (night).

Simulations of the FOV of hemispherical, downward-facing pyrgeometers at 270 positions show considerable variations in the measured L and inferred hemispherical radiometeric temperature $T_{0,\mathrm{h}}$ as a function of both horizontal placement and height. The root mean squared error (RMSE) between different horizontal positions in retrieving outgoing longwave emittance $L_\uparrow$ decreased exponentially with height, and was 11.2, 6.3 and 2.0 $\mathrm{W\,m^{-2}}$ at 2, 3, and 5 times the mean building height z_b. Generally, above $3.5\,z_b$ the horizontal positional error is less than the typical accuracy of common pyrgeometers. The average $T_{0,\mathrm{h}}$ over 24 h determined from the hemispherical radiometer sufficiently above an urban surface is in close agreement with the average $T_{0,\mathrm{C}}$. However, over the course of the day, the difference between $T_{0,\mathrm{h}}$ and $T_{0,\mathrm{C}}$ shows an RMSE of 1.7 K (9.4 $\mathrm{W\,m^{-2}}$) because the relative contributions of facets within the projected FOV of a pyrgeometer do not correspond to their fractions of the complete urban surface.

1 Introduction

The surface (or skin) temperature T_0 is a key parameter in the energy balance of land surfaces. It varies with time as a response to the radiative, conductive and convective energy transfers at the surface (Arya, 2008). The energy balance of built-up areas is altered compared to most natural vegetated land surfaces towards a higher storage of sensi-

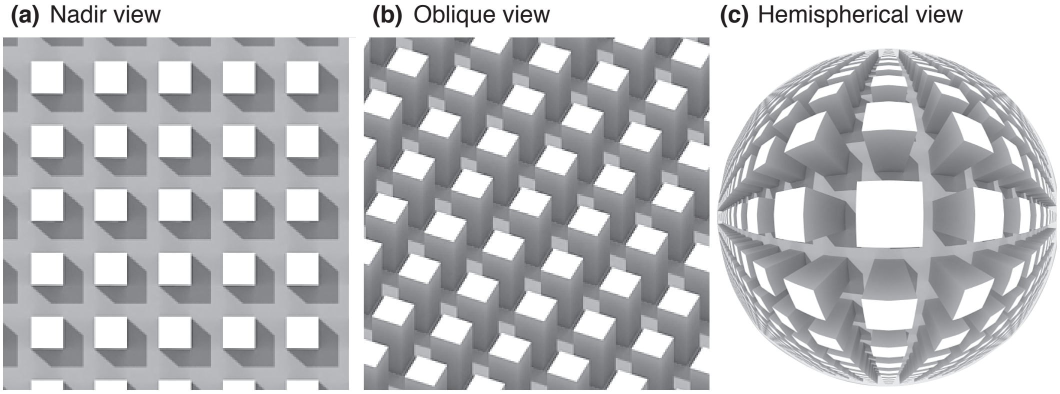

Figure 1. Projected field of views (FOV) for various sensor view geometries on a generic array composed of aligned blocks of width H, height $2H$ and an inter-element spacing H. The figure shows **(a)** a sensor with a narrow FOV in the nadir, **(b)** a sensor with a narrow FOV from an oblique view point and **(c)** a hemispherical radiometer facing downwards.

ble heat in the fabric, a shift in the partitioning of available energy from latent to sensible heat, and the release of additional energy by anthropogenic fuel combustion and electricity use (e.g. Oke, 1982; Cleugh and Oke, 1986; Christen and Vogt, 2004; Offerle et al., 2006). In addition, the convoluted, three-dimensional urban surface traps shortwave (solar) and longwave (terrestrial) radiation through multiple reflections (Oke, 1981; Harman et al., 2004; Krayenhoff et al., 2014). Any urban facet may receive emitted and reflected radiation from other facets comprising the urban surface. For most urban facets, the view factor of the sky ψ_{sky} is less than unity and the remainder are view factors of neighbouring urban facets (Johnson and Watson, 1984). Due to these alterations in the radiative, conductive and convective energy transfers, T_0 of urban systems is generally elevated compared to vegetated natural or agricultural surfaces in a city's surrounding. This phenomena is known as the surface urban heat island (SUHI). The SUHI is relevant to the energetics of buildings and for comfort of humans living in cities. It further establishes an altered boundary condition at the land–atmosphere interface that influences atmospheric energetics and dynamics in the urban boundary layer. This justifies our interest in retrieving T_0 of urban canopies routinely by means of ground- or satellite-based systems. Thermography infers T_0 using remotely measured longwave radiation from the surface of interest. A quantification of T_0 based on remotely sensed radiance (i.e. the received longwave radiation flux L by sensor per unit solid angle), however, is complicated in an urban setting by the following three factors.

Firstly, converting longwave radiance to a temperature by inverting the Stefan–Boltzmann Law yields a brightness temperature T_{B}, which is not necessarily equal to the true surface temperature T_0. If the surface is a grey body, knowledge of the surface emissivity ε and incoming longwave radiation is required to translate T_{B} into T_0. The surface emissivity varies widely with materials in urban systems (Kotthaus et al., 2014) as does incoming longwave radiation on different facets as not only sky radiation, but also emittance from neighbouring facets is intercepted. Differences in emissivities in urban systems can cause differences of up to 7 K between T_{B} and T_0 (Voogt and Oke, 1997).

Secondly, the radiance recorded with distant sensors is affected by atmospheric effects, where absorption and re-emission of longwave radiation from gases and aerosols between sensor and ground surface will affect measured T_{B} (Meier et al., 2011). Generally, this affects satellite sensors to a larger extent than airborne or ground-operated sensors due to the increased path length between sensor and surface d_{s}. A correction requires detailed knowledge of d_{s}, T_{a} and composition of the intervening atmosphere.

Thirdly, surface temperatures of various facets $T_{0,\mathrm{f}}$ (e.g. walls, roofs, roads) vary considerably due to differences in the facet-specific energy balance, which in turn are caused by different local solar zenith angles, shading, view factor heterogeneity, thermal/radiative surface property differences and moisture availability in an urban canopy. While the definition of T_0 of a flat and homogeneous surface is straightforward, it is more challenging to define an integrated surface temperature of a convoluted urban canopy. The complete surface temperature $T_{0,\mathrm{C}}$ can be approximated as the area-weighted $T_{0,\mathrm{f}}$ of all facets that compose an urban surface. More precisely we define it here as the surface temperature calculated from the area-weighted longwave outgoing radiation of all facets of the urban surface (Voogt and Oke, 1997), which in absence of reflection ($\varepsilon = 1$) leads to the following:

$$T_{0,\mathrm{C}} = \sqrt[4]{\frac{\sum_f A_{\mathrm{f}} T_{0,\mathrm{f}}^4}{\sum_f A_{\mathrm{f}}}}, \tag{1}$$

where A_{f} is the surface area of any given facet f. To compute $T_{0,\mathrm{C}}$, a detailed description of all facet surface temperatures $T_{0,\mathrm{f}}$ is required; hence $T_{0,\mathrm{C}}$ is rarely determined in detail.

Any narrow FOV or hemispherical radiometer located at a fixed location inherently exhibits a biased view of the 3-D urban surface. Here, a narrow FOV sensor is defined as a pinhole camera at infinite distance that covers a radiometric source area that is a representative patch of an urban canopy for the given off-nadir angle (ϕ) and azimuthal viewing direction (Ω). It is used to represent the view of a pixel in a satellite overpass. A hemispherical sensor is a sensor with a FOV of 2π with a cosine response. A typical example is the signal of a downward-facing pyrgeometer. Figure 1 illustrates three typical views of a generic "urban" array. The views correspond to the projected FOV of a narrow FOV sensor in the nadir (Fig. 1a), a narrow FOV sensor with an oblique view direction (Fig. 1b) and the view of a hemispherical radiometer facing down (Fig. 1c).

Note that the view area of roofs, walls, ground and shadows is different between the three projected FOVs in Fig. 1. Consequently, if walls, roofs, ground and shadows have different $T_{0,\mathrm{f}}$, the observed facet temperature of any biased view ($T_{0,\mathrm{d}}$) integrated over its FOV is not necessarily equal to the simultaneously observed $T_{0,\mathrm{d}}$ of other view directions and can also be different from $T_{0,\mathrm{C}}$ (Voogt, 2008). This effect, caused by the thermal anisotropy of the canopy in combination with a biased sampling in the projected FOV, affects airborne and satellite sensors as well as hemispherical radiometers (Voogt and Oke, 2003). Voogt and Oke (1998) found that this measurement error due to biased views combined with the thermal anisotropy of the surface exceeds that introduced by emissivity and atmospheric effects over urban surfaces (up to 10 K from anisotropy compared to 1.5–2.5 and 4–7 K from emissivity and atmospheric effects, respectively). The error becomes increasingly large as sensors deviate from the vertical, as is often the case with airborne and satellite sensors that have off-nadir viewing capabilities. Selected studies have attempted to quantify this effect (Lagouarde et al., 2004; Voogt, 2008; Lagouarde et al., 2010) for given cities using airborne measurements from different views. Nevertheless, most applications and studies simply neglect the resulting errors of radiometer placement and view direction on remotely sensed surface (brightness) temperatures of urban systems.

The goal of this contribution is to quantify the error in terms of a difference between directional radiometric temperatures ($T_{0,\mathrm{d}}(\phi,\Omega)$) and $T_{0,\mathrm{C}}$ in absence of emissivity effects, for varying ϕ and Ω of a typical urban system. A second goal is to make recommendations for the placement of hemispherical radiometers in order to best capture "representative" upwelling longwave radiation.

2 Methods

The proposed method uses panoramic time sequential thermography (PTST) data (Sect. 2.1) and a digital urban surface model (Sect. 2.2) to reconstruct $T_{0,\mathrm{f}}$ over time of all relevant urban facets (Sect. 2.3). This data set is then used to calculate $T_{0,\mathrm{C}}$ of the convoluted urban canopy and to simulate biased views of narrow FOV radiometers and hemispheric radiometers using computer graphics methods (Sect. 2.4). Based on $T_{0,\mathrm{f}}$, emittance is simulated and the receipt of radiation is modelled for various biased views at different locations.

2.1 Panoramic time sequential thermography

2.1.1 Site

The PTST data were obtained from a thermal camera on top of a mobile hydraulic mast installed in a relatively uniform suburban area (Sunset neighbourhood) of Vancouver, BC, Canada. This area has various long-term instrumentation for urban climate monitoring in place, including measurements of radiative and convective fluxes on top of a 26 m long-term flux tower named "Vancouver-Sunset" (Christen et al., 2013). The area is characterized by detached houses (Local Climate Zone 6, Stewart and Oke, 2012) following an orthogonal street grid layout. Measurements and modelling took place in the 6100 block of Elgin Street between E 45th and E 46th Ave (49°13′42″ N, 123°05′02″ W, WGS-84), located 500 m to the NW of the "Vancouver-Sunset" flux tower. The selected canyon section has a total of 12 buildings uniformly aligned along a north–south road, which minimizes asymmetric solar irradiance interactions over the course of a day. The lack of tall vegetation in the canyon section simplifies the projection of measured longwave emittance from the PTST data set on to a urban surface model (USM) and reduces the geometric complexity and uncertainties associated with the movement of trees in wind. The canyon section studied had a canyon width of 33.3 m. A concrete road of 13 m width was located roughly in the centre of the canyon bounded with lawns (and sidewalks) on both sides. Houses in the canyon were all built between 1971 and 1976 and are of similar dimensions and materials, with a rectangular footprint oriented perpendicular to the street and low-pitched roofs with slopes from 10 to 15°. Building peak heights vary from 6.2 to 7.1 m in a two-floor configuration, with an area-averaged roof area height of 6.23 m. Total building volumes range from 520 to 750 m^3. Most buildings have extensive back porches often with a carport towards a 6 m wide back lane (asphalt, concrete and bare soil). The relative uniformity of the structures simplified the complex geometry and proved helpful when statistically filling obstructed areas. The model domain encompassed a west–east (cross-canyon) extent of 90 m and a north–south (along-canyon) extent of 92 m (Fig. 3).

2.1.2 Instrumentation

A pan and tilt device allowed the camera to record 360° scans at different tilt angles over the course of a 24 hour cycle at a temporal resolution of 60 min. The field of view (FOV) of the PTST data set corresponds roughly to that of a downward-

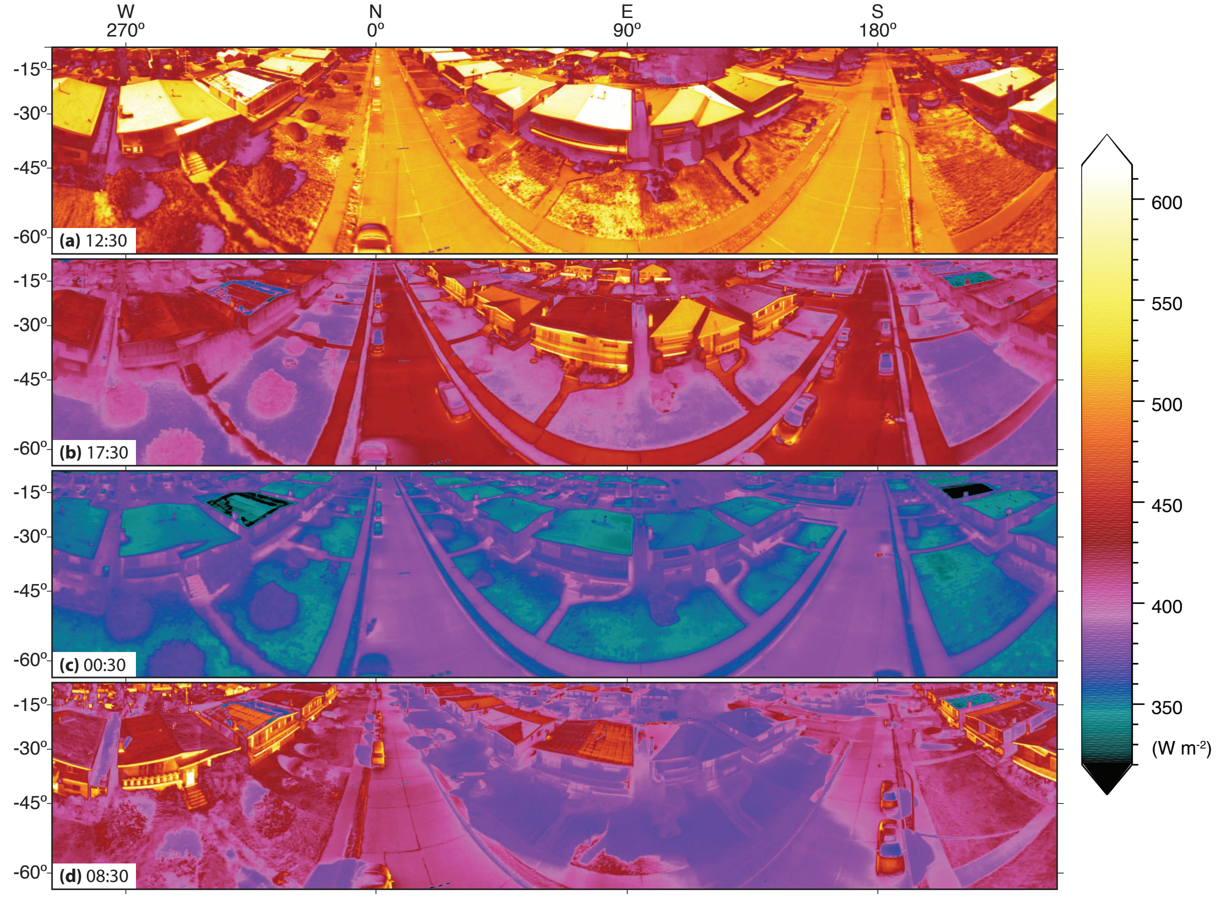

Figure 2. Selected time steps of the panoramic time sequential thermography (PTST) data set for 14 September 2008, 12:30 **(a)**, 17:30 **(b)** and 15 September 2008, 00:30 and 08:30. Each panorama is composed of ≈ 120 single images and projected using a conformal Mercator grid relative to the local horizon. See Supplement for PTST data from additional time steps.

facing hemispherical radiometer. In contrast to a radiometer that returns a single, integrated value over time, the spatially resolving PTST covers the lower hemisphere with $> 4 \times 10^4$ pixels over time (Fig. 2).

A Thermovision A40M thermal infrared camera (FLIR Systems, Wilsonville, Oregon, USA) with a wide angle lens was mounted atop a mobile hydraulic mast in the centre of the canyon studied at a height of 17.95 m above ground level (2.88 z_b). The system has a FOV of 61° × 48° corresponding to 320 by 240 pixels. Every hour, the camera was rotated in a 360° panorama at two different tilt angles, one at approximately 65° off-nadir, another at approximately 45° resulting in panoramic scans with a spatial resolution of 1.07×10^{-5} sr, which corresponds to panoramas of $>$ 40 M pixels per scan. The panorama omitted a cone directly in the nadir, where the mast was located. Details of the scan pattern can be found in Adderley (2012).

The Thermovision A40M uses an uncooled microbolometer sensor to retrieve T_B from measurements of incoming longwave radiation. The microbolometer is sensitive to thermal infrared radiation between 7.5 to 15 µm although highest sensitivity is concentrated between 9.2 and 11.8 µm ($>$ 90 % sensitive). The detectors have a radiometric resolution of 16 bits/pixel. At ambient T_0 near 300 K, a sensitivity of 0.08 K is achievable, with an absolute accuracy of ± 2 K (Flir Systems, 2004). Data from the thermal camera were recorded in digital format via FireWire on a PC. Each panoramic scan resulted in 250 frames at 320 by 240 pixels.

Two tripods with meteorological sensors were deployed to the north of the hydraulic mast on lawns to the east and west of the street and provided measurements of air temperature T_a and relative humidity RH at 0.3 m (HMP-35, Campbell Scientific Inc., Logan, UT, USA). Those were used for atmospheric correction (see Sect. 2.3). Additionally, at "Vancouver Sunset" (49°13′34″ N 123°04′42″ W, WGS-84), a CNR1 4-Component Radiometer (Kipp and Zonen, Delft, Netherlands) provided measurements of hemispherical radiation fluxes at 26 m above the surface. Shortwave irradiance ($K_\downarrow$), and reflected shortwave radiation ($K_\uparrow$) were measured using two CM3 pyranometers, and longwave irradiance ($L_\downarrow$), and the sum of emitted and reflected longwave radiation ($L_\uparrow$)

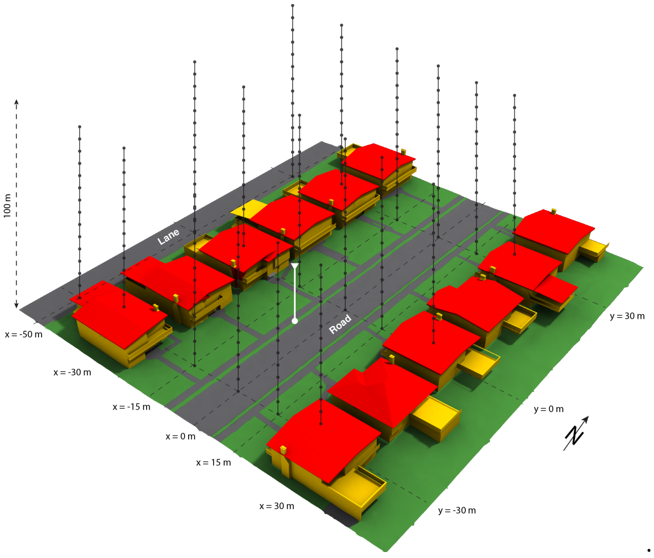

Figure 3. Rendering of the modelled urban canyon with facet classifications (roofs: red, walls and other building structures: yellow, lawns: green, roads and pathways: grey), location of the hydraulic mast (white line) and the thermal camera (white triangle). The vertical black dots refer to the 270 simulated positions of hemispherical radiometer locations (see Sect. 3.3)

were quantified using two CG3 pyrgeometers (spectral sensitivity from 5 to 50 µm), all at 5 min temporal resolution.

2.1.3 Study period

Observations were made between 14 September 2008 at 13:30 and 15 September 2008 at 12:30. The weather during the field campaign was cloud free. A cloud-free situation with direct-beam irradiance maximizes thermal anisotropy and is usually the situation when thermal remote sensing is performed. During the study period, air temperatures ranged between 284.7 and 298.5 K in the canyon. Daily total measured $K_{\downarrow}$ was 31.9 MJ m^{-2} day^{-1}, of which 4.9 MJ m^{-2} day^{-1} was reflected ($K_{\uparrow}$). Daily total measured $L_{\downarrow}$ was 29.4 MJ m^{-2} day^{-1}, and $L_{\uparrow}$ was 37.1 MJ m^{-2} day^{-1}.

2.2 Urban surface model

A highly detailed 3-D urban surface model (USM) of the urban surface was constructed based on detailed surveying data.

2.2.1 Geometric information

Basic positional information of the urban surface was collected with a Trimble R7 differential GPS (DGPS) unit (Trimble, Sunnyvale, California, USA), with horizontal position accuracy < 1 cm and vertical accuracy < 2 cm. The DGPS data were supplemented with Light Detection and Ranging (LiDAR) data flown during March 2007 by a fixed wing aircraft operating a TRSI Mark II discrete-return sensor (Goodwin et al., 2009). For the purposes of this project, only the ground returns of the LiDAR were used. Close-range photogrammetry was chosen to reconstruct buildings. In close-range photogrammetry, multiple images from varying directions of the same building are correlated to solve 3-D positions of points and lines. These features are then assembled into vector representations of buildings. The images collected for photogrammetry were taken at ground level and from atop the same hydraulic mast at multiple locations using a Nikon D100 digital single-lens-reflex (SLR) camera (Nikon, Tokyo, Japan), equipped with a 28 mm Nikkor lens. Eos Photomodeler (Version 6.2, Eos Systems, Vancouver, BC, Canada) was used to reconstruct vector building models from digital SLR images. Eos Photomodeler has been used previously for modelling of urban form with good performance (Nikiforiadis and Pitts, 2003). The street canyon was broken down into its component features, with each house being modelled individually, and then integrated together in 3-D Studio Max (Version 8, Autodesk, San Raphael, CA, USA) to form a complete canyon 3-D model. The resulting USM is visualized in Fig. 3 in form of a 3-D projection.

2.2.2 Facet and material information

The material type defines the emissivity ε of a facet (Oke, 1987) and other underlying material properties (e.g. thermal admittance). A survey of the ground-level photos and orthophotography was undertaken, creating an inventory of all material types in the canyon (Table 1). Materials were manually marked on the triangles composing the USM using a material identifier code. Where material boundaries did not fit the topology of the model, additional triangles were added in order to correctly attribute materials. To each of the materials, a ε value was attributed based on Flir Systems (2004). It was assumed that ε is isotropic; i.e. surfaces show a Lambertian behaviour in the longwave band. Also aging and weathering of surfaces was not considered in the attribution of ε to materials.

2.2.3 Sky view factor

The sky view factor (ψ_{sky}) was calculated for each surface pixel using an ambient occlusion algorithm in 3-D Studio Max. In ambient occlusion, each pixel on a 3-D model is the source for a Monte Carlo ray casting simulation, where sampling rays are cast in all directions from the pixel with a cosine probability relative to the zenith. To test the ability of ambient occlusion algorithms to numerically determining ψ_{sky} in complex geometries, several idealized 3-D situations in which ψ_{sky} was known were compared against this algorithm. The results showed good correspondence with a maximum error in ψ_{sky} of 0.02, indicating that the ambient occlusion method was adequate (Adderley, 2012).

Table 1. Inventory of materials found in the Elgin Street canyon with attributed emissivities (Flir Systems, 2004), and relative frequency in % of complete surface.

Material	Emissivity ε	Fraction of complete surface (%)		
		Roofs	Walls	Ground
Aluminum	0.70	6.9	0.6	0.0
Asphalt/tar	0.97	7.4	0.0	0.0
Brick	0.93	0.0	0.9	0.0
Concrete	0.92	0.0	0.1	9.4
Glass window	0.80	0.0	3.0	0.0
Grass	0.95	0.0	0.0	49.9
Paint	0.93	0.7	18.6	0.0
Rock	0.82	0.0	0.4	0.0
Stucco	0.91	0.0	2.0	0.0
All		15.1	25.6	59.2

2.3 Projecting measured T_B on surface

Using coordinate transformation, measured T_B from each frame pixel in the PTST data were projected on the USM. As a first step, the three-dimensional vector-based USM was decomposed into planar bitmap images by assigning a set of planar 2-D coordinates to each face of the model (UVW mapping, Shirley et al., 2009). Cartesian coordinates of all pixels (x_s, y_s, z_s) were translated to global spherical coordinates where θ_s and ω_s are the spherical tilt and azimuth angles of a pixel relative to the camera location, and d_s is the distance of that pixel to the camera location. Texture maps of θ_s, ω_s and d_s were also stored for all building and ground objects. Then each thermal camera frame pixel was interactively projected onto the 3-D USM, using a search algorithm that matched θ_s and ω_s of the PTST data set to θ_s and ω_s of the USM. Manual inspection of projected panoramas revealed some areas of incorrect attribution along edges and on distant objects. Those areas were eliminated manually and filled using a gap-filling algorithm. Details of this procedure are described in Adderley (2012)

2.3.1 Atmospheric correction

Atmospheric correction were performed for each time step after projecting T_B back onto the USM. A set of MODTRAN simulations were run for the current camera spectral range following the procedure outlined in Meier et al. (2011). These corrections considered path length (d_s), local air temperature (T_a, measured in canyon), sensor measured brightness temperature T_B and relative humidity RH (measured in canyon). Due to the large number of T_a, T_B and path length values, it was impractical to run a MODTRAN simulation for each combination. Instead, a number of scenarios were run by changing T_B at 5 K intervals (for range 278–323 K), T_a in 2 K intervals (273–303 K), RH at 2 % intervals (40–80 %), and d at intervals of 10 m (15–75 m). The resulting look-up table was interpolated linearly between two T_B values to match the actual T_B of each pixel, while for all other parameters the nearest value was used. Corrections of individual pixels ranged between 0.7 and 8.6 K (road, midday, large d_s) over the 24 h.

2.3.2 Emissivity correction

To retrieve each pixel's $T_{0,\mathrm{px}}$ from measured $T_{\mathrm{B,px}}$ we used the broadband equation showing that longwave flux density $L_{\uparrow,\mathrm{px}}$ observed from a surface is the sum of emittance and longwave reflected radiation (Oke, 1987):

$$L_{\uparrow,\mathrm{px}} = \sigma T_{\mathrm{B,px}}^4 = \varepsilon_\mathrm{px} \sigma T_{0,\mathrm{px}}^4 + (1-\varepsilon_\mathrm{px}) L_{\downarrow,\mathrm{px}}, \tag{2}$$

where ε_px is the pixel's emissivity previously attributed based on material. Equation 2 was then solved for $T_{0,\mathrm{px}}$:

$$T_{0,\mathrm{px}} = \sqrt[4]{\frac{\sigma T_{\mathrm{B,px}}^4 - (1-\varepsilon_\mathrm{px}) L_{\downarrow,\mathrm{px}}}{\sigma \varepsilon_\mathrm{px}}}. \tag{3}$$

A pixel's incoming longwave radiation $L_{\downarrow,\mathrm{px}}$ is approximated as the sum of longwave radiation from the sky weighted by the pixel's sky view factor (ψ_sky), and the longwave radiation from the canyon, weighted by the pixel' ground view factor ($1-\psi_\mathrm{sky}$).

$$L_\downarrow = \psi_\mathrm{sky} L_\mathrm{sky} + (1-\psi_\mathrm{sky}) \sigma T_{0,\mathrm{C}}^4 \tag{4}$$

L_sky is the directly measured incoming broad-band longwave radiation at the tower "Vancouver Sunset" for the given time step. The approximation in Eq. (4) assumes that atmospheric irradiance is isotropic, and that the surrounding urban facets all have a uniform surface temperature equal to $T_{0,\mathrm{C}}$. In this equation we first approximate $T_{0,\mathrm{C}}$ by $T_{\mathrm{B,C}}$. The correction was iteratively applied as the temperature correction changes the value of $T_{0,\mathrm{C}}$. This correction was performed repeatedly until the corrected surface temperature $T_{0,\mathrm{px}}$ for one iteration was not significantly different from $T_{0,\mathrm{px}}$ for the previous iteration (difference of less than 0.25 K). This was accomplished within 5 iterations.

2.3.3 Obstructed surfaces

As the thermal camera is at a fixed location, it is evident that not all pixels in the texture maps can be seen by the camera. Secondly, selected areas were removed by manual inspection because of minor misalignments along edges. The mean visibility of roofs and ground in the entire domain are 95 and 72 %, respectively. The visibility of E–W walls is only 46 % (lane-facing walls of buildings cannot be seen). For N–S walls, the visibility is good in the four nearest houses ($\approx$ 90 %); however it is very poor ($<$ 10 %) for all houses further away from the thermal camera. Hence, the PTST data set is also a preferred view; however its panoramic nature means that it contains data from all relevant facets of the urban canopy. However for simulating alternative projected FOVs the USM needs to be populated on all sides with temperatures.

The gap filling of unseen pixels was based on an adaptive search algorithm. For each pixel requiring interpolation, four predictors were extracted: the pixel facet type (roof, wall, ground), pixel material type, pixel orientation (azimuth and slope) and pixel ψ_{sky}. Each of these factors affects T_{B} of a surface. A search algorithm then looked at all measured pixels in the same texture sheet that matched the features to those belonging to the pixel to be filled. Matched pixels had to have identical facet type and material to the originating pixel. Sky view factor and orientation had variable thresholds: the orientation threshold was based on the slope of the pixel. Pixels with a high slope required an orientation value that was very close (within 5°), while pixels with a low slope had a more relaxed threshold (within 15°). The pixels used to statistically fill the obstructed target pixel had to experience a difference in ψ_{sky} of less than 0.03.

If similar pixels could not be found on the same object (i.e. house), the sheets for all other houses and the ground were examined. This was key in areas where only one side of the house was visible to the thermal image, as pixels for the opposite side would all be unattributed. This gap filling assumes that the houses have similar thermal behaviour in each direction from the tower. The same wall orientation is visible on the other side of the scanning camera (i.e. panorama) and houses with pixels matching the orientation could be always found. If similar pixels were still not found, the ψ_{sky} and orientation thresholds were relaxed by 5 %, and the search was repeated. In this way all pixels were matched.

2.4 Simulating the view of different radiometers

In order to examine the effect of biased view directions, the corrected surface temperature of each pixel ($T_{0,\text{px}}$) encoded in UVW texture form was first translated to a longwave emittance from the pixel ($L_{\text{px}} = \sigma T_{0,\text{px}}^4$), removing any emissivity effects in the simulation. Sensors were rendered using different angles and camera models using ray tracing simulations in 3-D Studio Max. Two sensor types were rendered: a simulation of a narrow FOV sensor representing a typical airborne or satellite radiometer (Sect. 2.4.2) and a simulation of a hemispherical downward-facing pyrgeometer with a FOV of 2π (Sect. 2.4.3). Atmospheric effects of intervening gases and aerosols were not considered in the simulations of the sensors. This way, any differences of biased views are solely caused by geometric effects in the absence of emissivity and atmospheric effects.

To represent L_{px} at sufficient resolution, texture maps of 32-bit true colour images were generated for the three-dimensional surface and imported into 3-D Studio Max. This was necessary as the number of data values exceeds the range available using a traditional 8-bit greyscale map (256). With a 32 bit red, green, blue and transparency (RGBA) image, the number of possible data values is extended to $> 4 \times 10^9$, which is easily sufficient for representing flux densities at the thermal camera data depth. The number of unique L_{px} values present in the entire street canyon for a given time step were counted, sorted by magnitude, and indexed, with each value assigned an RGBA value. An image was created by matching the RGBA values to the L_{px} values for each map and exported into portable network graphics (PNG) images for each time step along with indexing data containing the transformation from L_{px} to colours. These PNG images were then imported and assigned to the correct facets of the 3-D USM in 3-D Studio Max. This converted the thermal data, split by texture maps, into a 3-D polygonal structure which could interact with the software's lighting and ray tracing engines for view direction simulations.

All rendered visual quality enhancements in 3-D Studio Max were disabled in order to avoid any filtering. Each sensor's projected FOV was rendered to a single frame 256 × 256 pixel array of RGBA values and exported to a PNG image. This was determined a high-enough resolution to render truthfully all relevant facets of the urban surface even for sensors at the highest locations. The RGBA values were converted to pixel longwave values L_{px} through the use of the original lookup table. The 256×256 matrix of converted $L_{\text{px}}(x, y)$ values was then averaged to a single value of L_{px}. The scalar L_{px} was then converted to a black body surface temperature of the biased view, $T_{0,\text{d}}$, simulating the physical procedure when retrieving surface temperatures.

2.4.1 Cyclic domain

If a simulation of a sensor at a high altitude is desired, the single domain of 92 by 90 m is insufficient. The domain was therefore repeated in the x and y directions, to create an effectively infinite suburban residential area conserving the anisotropy of the measured area. The resulting domain was then repeated approximately 50 times in both horizontal directions (45 000 houses). Though not completely infinite, it approximates an infinite plane for the view directions as simulated for a hemispherical downwards-facing sensor. The tiled surface is not completely representative of a city: it has no east–west streets, but serves adequately as an idealized suburban surface with the given data set. The characteristics of the cyclic domain are summarized in Table 2.

2.4.2 Narrow FOV rendering

In 3-D Studio Max, a pinhole-type camera was placed facing downward at 10^4 m above the tiled surface. A FOV of 1° was used for the camera with rendered pixel dimensions of 256 by 256 pixels (Fig. 4a). These parameters approximate a sensor pointing down at nadir with a projected FOV of 30 m. For oblique views, the camera was angled so that each frame faced the same centre point of the tiled surface (but the pro-

Table 2. Morphometric parameters describing the simulated urban domain.

	Description	Value
z_b	Area-weighted building height	6.23 m
V_b	Building volume per domain area	2.65 $\mathrm{m^3\,m^{-2}}$
x_c	Characteristic street canyon width	33.3 m
y_c	Characteristic along-canyon inter-building spacing	3.23 m
λ_s	Street canyon aspect ratio (z_b/x_c)	0.18
λ_b	Plan area ratio of buildings	0.34 $\mathrm{m^2\,m^{-2}}$
λ_i	Plan area ratio of impervious ground	0.21 $\mathrm{m^2\,m^{-2}}$
λ_v	Plan area ratio of vegetation	0.55 $\mathrm{m^2\,m^{-2}}$
λ_c	Complete aspect ratio	3.61 $\mathrm{m^2\,m^{-2}}$

jected FOV was larger). Camera azimuths (Ω) from 0 to 360° at an interval of 30° were simulated with off-nadir angles (ϕ) from 0 to 70° at intervals of 10°. This resulted in a total of 96 different view simulations for each of the 24 hourly steps.

2.4.3 Hemispherical sensor rendering

Hemispherical sensors were rendered as circular areas with diameter 256 pixels (Fig. 4b). The sensor was positioned directly above several points in three different transects from west to east throughout the canyon. For each position, varying heights were chosen (Fig. 3), from 2 to 10 m (at 2 m intervals) and from 10 to 100 m at 4 m intervals (up to approximately $z/z_b = 10$). A total of 270 hemispherical radiometer positions were rendered for a total of four time steps (13:30, 18:30, 00:30, and 06:30). These 6 hour intervals gave a reasonable assessment of the canyon temperature patterns over time for the available computational time. The imported $L_{\mathrm{px,h}}$ was then corrected for angle-of-incidence effects (cosine response) and averaged to recover a single signal of L_{h} for each radiometer position. Similar to the narrow FOV sensors, the simulated hemispherical sensor signals consider only emittance, and treat the surface as a black body. Note that measured L_{h} from a real broad-band pyrgeometer at different heights would additionally be impacted by atmospheric effects between the surface and the measurement level that are not considered in the current study.

3 Results and discussion

3.1 Complete surface temperature

Area-weighted $T_{0,\mathrm{f}}$ for different facet types are calculated by weighting corrected surface temperatures of each pixel i in the texture sheets $T_{0,\mathrm{px},i}$ with by their pixel area A_{px}:

$$T_{0,\mathrm{f}} = \frac{1}{I\,N\,A_{\mathrm{T}}}\sum_i I_{\mathrm{f},i}\,A_{\mathrm{px},i}\,T_{0,\mathrm{px},i}\,, \tag{5}$$

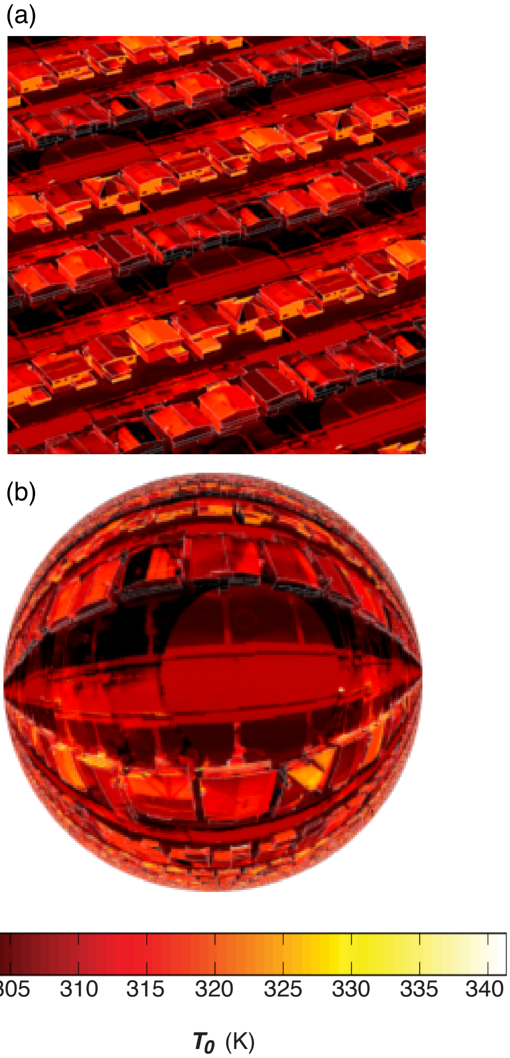

Figure 4. Examples of rendered **(a)** narrow FOV and **(b)** hemispherical radiometer rendering at 13:30.

where A_{T} is the complete total area of the 3-D model, N is the total number of pixels, and $I_{\mathrm{f},i}$ is an indicator function, which is equal to 1 if the pixel is attributed to facet type f and zero otherwise. I is the fraction of A_{T} that is attributed to facet type f (see Table 1).

To ensure a consistent comparison between $T_{0,\mathrm{C}}$ and simulated radiometer data averaged over the FOV of the instrument under study, $T_{0,\mathrm{C}}$ was calculated for each time step from each pixel's $T_{0,\mathrm{px},i}$ converted to a longwave emittance, and then averaging the longwave emittance and converting back to a brightness temperature, following Eq. (1):

$$T_{0,\mathrm{C}} = \sqrt[4]{\frac{1}{N A_{\mathrm{T}}}\sum_i A_{\mathrm{px},i}\,T^4_{0,\mathrm{px},i}}\,. \tag{6}$$

$T_{0,\mathrm{C}}$, and $T_{0,\mathrm{f}}$ of walls, roofs and ground are shown over the 24-hour cycle in Fig. 5.

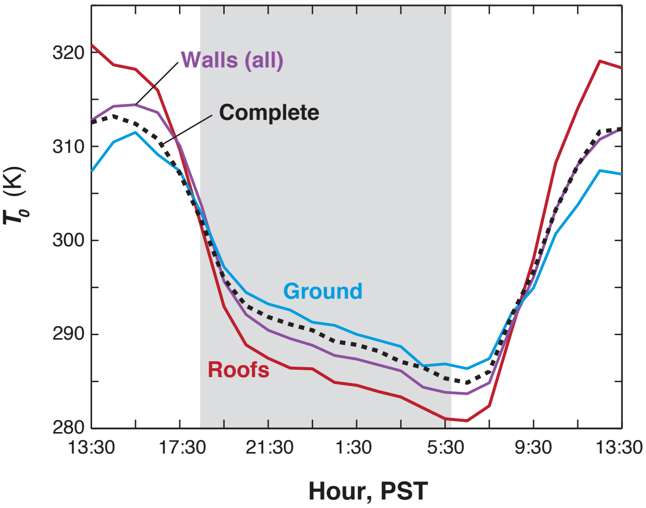

Figure 5. Area-weighted average $T_{0,\mathrm{f}}$ over the course of the field observations along with complete surface temperature $T_{0,\mathrm{C}}$. The shaded area is nighttime.

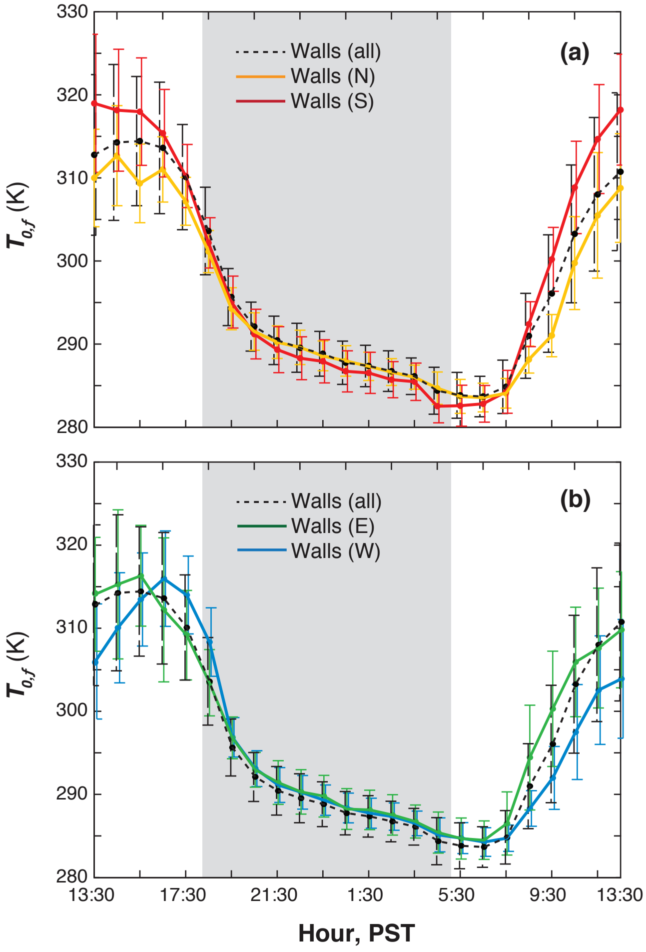

Figure 6. Area-weighted wall temperatures divided by facet orientation. Error bars show 1 standard deviation. **(a)** North- and south-facing walls. **(b)** East- and west-facing walls.

$T_{0,\mathrm{f}}$ of roofs display a distinct trend of higher values in the daytime with a spatial mean of 320.8 K (standard deviation ± 9.1 K) at 13:30, cooling down to lowest temperatures at night with a spatial mean of 280.8 K (± 2.5 K) at 06:30. Roofs will receive the most shortwave irradiance by day due to the lack of shading, and will cool rapidly by longwave emission at night due to their high ψ_{sky} and limited heat storage capabilities. Roof temperatures hence show the largest diurnal amplitude of 40 K (Table 3), which is in the typical range of reported values for clear-sky days in other studies (Masson et al., 2002; Chudnovsky et al., 2004; Christen et al., 2012; Salmond et al., 2012).

$T_{0,\mathrm{f}}$ of the ground facet shows the smallest diurnal range, with lowest $T_{0,\mathrm{f}}$ of all facet classes during the day with a maximum spatial mean of 311.5 K (± 3.35 K) at 14:30 and highest mean minimum $T_{0,\mathrm{f}}$ of all facets at night with 286.4 K (± 1.7 K) at 06:30. In-class variation is more limited than the roofs and is more constant over the entire data set, with minimal decrease at night. The ground facet has distinct material differences from roofs, being composed of 16 % concrete (road) and 84 % grass. Grass will not heat up as much by day due to transpirative cooling and consequently be cooled less at night. There was large spatial variability of grass temperatures due to different moisture availability (irrigation). For the road, we see warmer $T_{0,\mathrm{f}}$ at night in the canyon floor compared to roofs. The road tends to have an intermediate ψ_{sky} due to its location in the centre of the canyon and the receipt of longwave radiation from nearby walls will retard cooling in the canyon floor, compared to roof tops.

Walls exhibit a $T_{0,\mathrm{f}}$ between ground and roofs (Fig. 5) with a spatially averaged maximum of 314.4 K (± 7.8 K) at 14:30 and a minimum of 283.7 K (± 2.4 K) at 06:30. Figure 6 shows $T_{0,\mathrm{f}}$ split by facet orientation into four cardinal directions. Notably, south-facing walls achieve warmer 24 h temperatures of 298.5 K (± 4.0 K) than others due to their sun-facing aspect. At night, north- and south-facing walls are slightly colder than west- and east-facing walls (Table 3). This can be explained by the substantial roof overhangs and balconies that reduce the local sky view faction over the west- and east-facing walls and possibly the fact that east- and west-facing walls have more windows. Excluding the nighttime situation, the north-facing walls are cooler than the south-facing walls by an average of 5.6 K (± 3.6 K), which is to be expected considering the location of the sun at this time of the year. North-facing walls are only irradiated for $<$ 30 min near sunrise and sunset in cases where the solar altitude is $<$ 3.9° (substantial shading is expected). In summary, walls experience intermediate $T_{0,\mathrm{f}}$. During the day, $T_{0,\mathrm{f}}$ is highest for roofs, followed by walls and lowest for the ground. During night $T_{0,\mathrm{f}}$ is highest for ground, followed by walls and lowest for roofs.

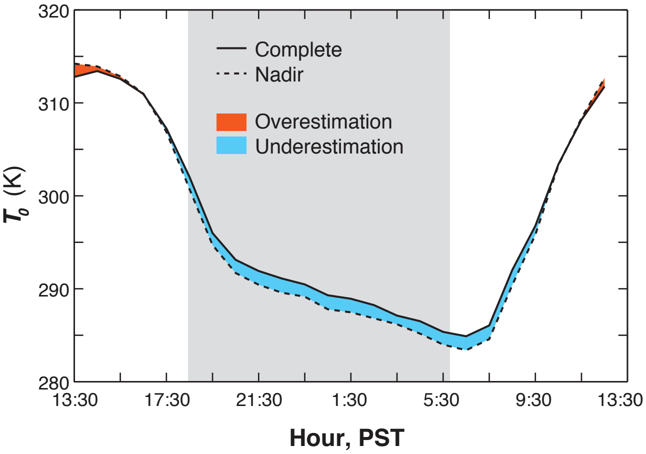

Figure 7. Diurnal course of $T_{0,\mathrm{C}}$ compared to $T_{0,\mathrm{d}}(\phi = 0)$ of a sensor with a narrow FOV in the nadir.

Table 3 separates the behaviour of canyon facets by type, material and orientation. In general, it is expected that the mean diurnal amplitude of $T_{0,\mathrm{f}}$ should be inversely related to the thermal admittance μ of the facet in question: low μ result in larger mean diurnal amplitudes. Roofs have lowest μ due to primarily low conductivities. Ground facets have reasonably high μ and reflect this in a low mean diurnal amplitude (25.1 K). The effect of orientation is evident for walls. North-facing walls having the lowest mean diurnal amplitude (29.1 K). The largest variation (south facing) shows the highest diurnal amplitude (36.5 K), and the east- and west-facing walls, which also have large variations in shading, show identical mean diurnal amplitudes (31.7 K).

3.2 Narrow FOV radiometers

3.2.1 Nadir view

Figure 7 compares the surface temperature inferred from a narrow FOV sensor at nadir ($T_{0,\mathrm{d}}(\phi = 0)$) to $T_{0,\mathrm{C}}$. $T_{0,\mathrm{C}}$ is lower than $T_{0,\mathrm{d}}(\phi = 0)$ in the daytime and is higher following sunset in a situation that favours strong radiative cooling (many facets with high ψ_{sky}, clear skies, both of which are present in this situation). The largest difference is present near solar noon (solar altitude 43°); at this time horizontal surfaces, especially those with large ψ_{sky}, are warm relative to vertical surfaces and dominate the radiance received by a narrow FOV sensor. The reverse is true at night, where wall $T_{0,\mathrm{f}}$ are likely to be higher (see Fig. 5) than $T_{0,\mathrm{f}}$ of horizontal facets, in particular those of roofs, due to their low thermal admittance.

A maximum difference $T_{0,\mathrm{d}}(\phi = 0) - T_{0,\mathrm{C}}$ of +2.0 K is observed at 13:30 (overestimation by the sensor), and values are closest at 10:30. Over the course of the day, the root mean squared error (RMSE) of $T_{0,\mathrm{d}}(\phi = 0) - T_{0,\mathrm{C}}$ is 1.2 K. Roberts (2010) compared $T_{0,\mathrm{C}}$ to $T_{0,\mathrm{d}}(\phi = 0)$ of a hardware scale model over the course of a day. The maximum overestimation $T_{0,\mathrm{d}}(\phi = 0) - T_{0,\mathrm{C}}$ is reported at solar noon and has a value of around +2.5 K, which is similar to this study (+2.2 K). During nighttime, the $T_{0,\mathrm{d}}(\phi = 0) - T_{0,\mathrm{C}}$ differences for the lowest density configuration in Roberts (2010) range between −0.5 and −1 K, which is again comparable to values found here (−0.9 to −1.4 K, underestimation).

3.2.2 Oblique view

The large number of view directions simulated allows the systematic examination of the difference between directional and complete surface temperatures for oblique sensor views. The difference $T_{0,\mathrm{d}} - T_{0,C}$ is plotted in polar form in Fig. 8. In these polar plots, each pixel represents a temperature value for a view direction as plotted by the off-nadir angle (ϕ) and azimuth from geographic north (Ω) of the sensor location. At the centre of the plot lies the value at nadir ($\phi = 0$).

In the daytime situations, the effects of anisotropy are clearly visible, particularly before solar noon (Fig. 8b). Here in half of the hemisphere, $T_{0,\mathrm{d}}$ underestimates $T_{0,\mathrm{C}}$ (opposed to solar position) and in the other half $T_{0,\mathrm{d}}$ overestimates $T_{0,\mathrm{C}}$ (same side as solar position – the solar position is represented by a cross in 8b). Generally over the day, the hotspot of highest $T_{0,\mathrm{d}}$ is following the solar position (see also Supplement). When the position of the sun is close to the direction of the sensor, the signal is mostly overestimated. The daytime hotspot has a slight lag from the sun's position (approximately 1 h).

This pattern of higher visible $T_{0,\mathrm{d}}$ from the direction of the sun persists until the sun moves below the horizon (by 17:30) at which point the difference between west and eastern facets begins to be reduced, but is still sustained a few hours (Fig. 8, right). By 18:30, most modelled views show a $T_{0,\mathrm{d}}$ lower than $T_{0,\mathrm{C}}$. The south-facing regions remains warm due to residual heat stored that is now released.

Moving into the nighttime, a continued decay of the daytime hotspot is evident until 21:30 (see Supplement). Until this point, views from the south continue to be consistently warmer, underestimating $T_{0,\mathrm{C}}$ by only 0.5–1.1 K. For most other views, there is a consistent underestimation of $T_{0,\mathrm{C}}$ by $T_{0,\mathrm{d}}$ by between −1.0 and −2.2 K. Generally, anisotropy is lower at night. After the hotspot disappears, most of the view directions show similar values for a given ϕ. Moving onto the morning, a hot spot develops in intensity by 08:30 and causes very large $T_{0,\mathrm{d}}$ to $T_{0,\mathrm{C}}$ differences of −2.4 K when looking from the west.

Throughout all simulations, we find overestimations of $T_{0,\mathrm{C}}$ by $T_{0,\mathrm{d}}$ of up to +2.9 K (17:30) and underestimations by up to −2.6 K (08:30) (Fig. 9). The simulated values of $T_{0,\mathrm{d}}$ can be also used to determine the anisotropy (maximum temperature difference between the most extreme view directions), which is the distance between the minimum and maximum whiskers in Fig. 9.

Table 3. Summarized area-weighted mean maximum and minimum surface temperatures with calculated mean diurnal amplitude for canyon materials, divided by facet type and orientation. Values in brackets show standard deviations.

Facet type	Mean maximum temperature (K)	Mean minimum temperature (K)	Mean diurnal amplitude (K)
Roofs (all)	320.8 (± 9.1)	280.8 (± 2.5)	40.0
asphalt only	321.0 (± 6.2)	280.9 (± 1.8)	40.1
metal only	294.8 (± 10.9)	257.5 (± 2.3)	37.3
Ground (all)	311.5 (± 3.4)	286.4 (± 1.7)	25.1
grass only	309.3 (± 3.1)	284.6 (± 2.0)	24.7
concrete	317.6 (± 3.1)	287.8 (± 1.6)	29.8
Walls (all)	314.4 (± 7.8)	283.7 (± 2.4)	30.7
North-facing walls	312.7 (± 6.0)	283.6 (± 1.7)	29.1
South-facing walls	319.0 (± 8.3)	282.5 (± 2.0)	36.5
East-facing walls	316.3 (± 6.0)	284.6 (± 2.3)	31.7
West-facing walls	316.0 (± 5.7)	284.3 (± 1.7)	31.7

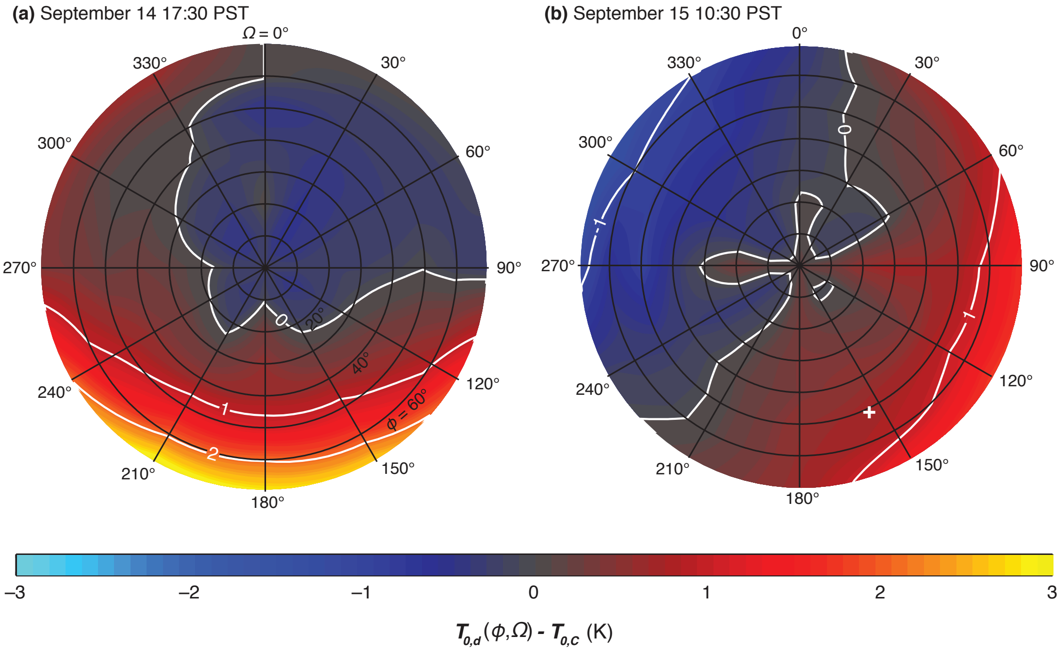
(a) September 14 17:30 PST

(b) September 15 10:30 PST

Figure 8. Examples of the bias $T_{0,\mathrm{d}}$–$T_{0,\mathrm{C}}$ for sensors with a narrow FOV in the nadir and various oblique angles 1 hour after sunset (left, 17:30) and in the late morning (right, 10:30). The white cross shows the relative position of the solar disk at this time. Graphs for all other hourly time steps can be found in the Supplement to this article.

The effective anisotropy shows expected behaviour following observational results from Voogt and Oke (1997), with high anisotropy in the daytime (up to 3.5 K) and little anisotropy at night (< 1.0 K). The trend also follows that of the residential neighbourhood in Voogt and Oke (1998), which showed higher differences in measured brightness temperatures from differing view directions in morning and late afternoon situations (10:00 and 17:00) compared to midday situation (14:00). Magnitudes are similar as well though the simulated Elgin Street anisotropy is lower by approximately 1.5 K at 10:00 and 17:00. All of these studies took place in Vancouver neighbourhoods with similar urban structure, so an agreement is expected and supports the findings here. Aircraft measurements of thermal anisotropy from Marseille, France in Lagouarde et al. (2004) also follow this trend, with maximum anisotropy during the morning (08:00 to 10:00). However, their anisotropy is much larger (up to 10.5 K) likely due to the different urban form and fabrics, different thermal sensor types, and potentially also differences in the ratio of direct to diffuse shortwave irradiance.

3.3 Hemispherical sensor

Figure 10 shows simulated signals of longwave emittance L_h measured by a hemispherical sensor (i.e. a downward-facing

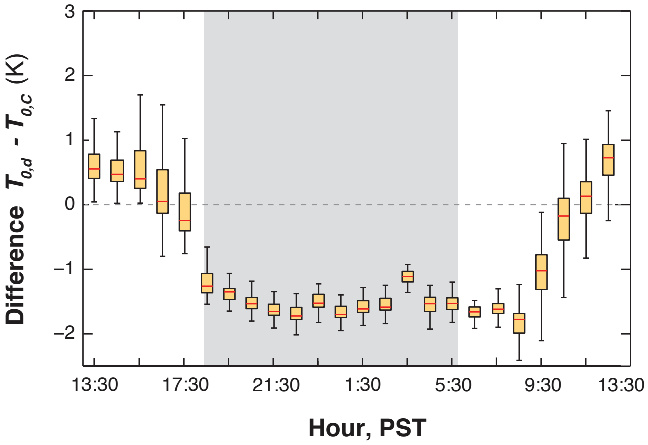

Figure 9. Deviation of all simulated view direction temperatures from $T_{0,\mathrm{C}}$ by time step. The box plot show minimum, maximum (whiskers), 5 and 95 % percentiles (boxes) and median values (bars).

pyrgeometer) at various locations above the canyon for the mid-day and a midnight time step.

3.3.1 Daytime case

At 13:30 there is a strong variation in L_h with pyrgeometer position across the canyon as indicated by the different coloured profiles in Fig. 10a. The 18 profiles converge near 500 W m^{-2} at $z/z_b = 7.5$ to a RMSE between all profile locations at the same height of less than 1 W m^{-2}. The pattern of variability between sensor positions across the canyon cross section is repeated for all three canyon slices ($y = -30, 0, 30$ m, see Fig. 3) with only minor differences.

Below z_b, pyrgeometer positions over lawns exhibit lower L_h (lower T_0 due to transpirative cooling of lawns that cover the largest view fraction in the FOV). The pyrgeometer positions on opposite sides of the street exhibit different behaviour: the positions over the western lawn experience higher L_h due to the warmer nearby house east-facing walls and also the warmer grass temperatures on the west lawns at noon (2.5 K warmer than lawns on east side). West lawns and the east-facing walls receive more incoming shortwave radiation during the morning when they are not shaded. For the pyrgeometer positions over the eastern lawn, L_h increases continuously with height, particularly above $z/z_b = 1.0$, as at this point roofs will begin to contribute to the sensor view. Being substantially warmer than lawns, the roofs will increase the measured L_h. The western lawn shows a different pattern, with rapidly increasing L_h until $z/z_b = 1.5$ at which point L_h beings to decrease with height.

The profiles of simulated pyrgeometer positions over road and lane facets are behaving roughly similar, with the road having slightly higher temperatures due to a larger area covered by concrete being present and the higher ψ_sky of this position compared to the simulated lane. This causes L_h over the road at low z/z_b to be larger. For the lane, its lower ψ_sky will reduce heating due to lower solar irradiance (shadowing). In addition, facets visible in the lane include recessed areas such as garages and porches which receive less irradiance throughout the entire day. We would expect these recessed areas to reduce overall L_h. Both road and lane locations show a decrease in L_h with height.

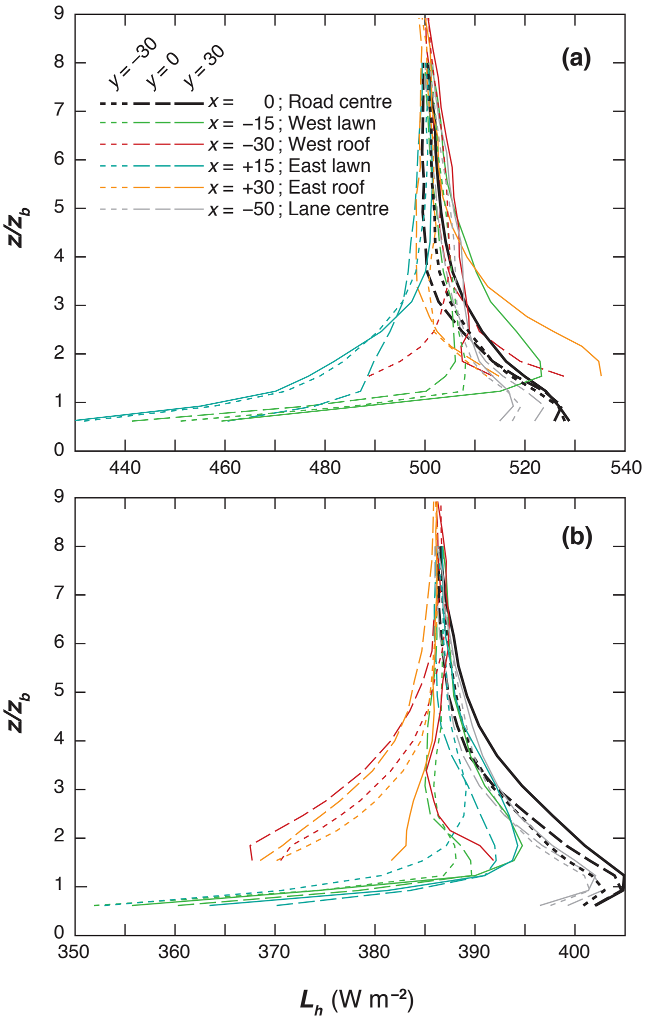

Figure 10. Simulated signals for L_h retrieved from hemispherical sensors (pyrgeometers) at various heights and locations for **(a)** 14 September 14:00 and **(b)** 15 September 00:30. Each graph represents a vertical profile above a specific canyon location as shown in Fig. 3. Note the different scales of the x-axis in panels **(a)** and **(b)**.

Directly above the roofs, L_h varies greatly across the canyon and for many positions is higher than the converged value far above the canopy, as the view factor comprises mostly hot roofs while walls are less visible. Roofs have been shown to be warmer throughout the experiment in the daytime (see Fig. 5), and also exhibit a range of different albedo and thermal admittance values and that explain differences along the canyon and between the east and west rows. Most profiles of L_h decrease rapidly with height. Only above-roof positions (those at $x = -30$ and $x = +30\,\mathrm{m}$) show larger variability of L_h with location in the along-canyon direction as opposed to the other positions (lawns, road). This variability is driven by differences in roof materials from house to house, with asphalt roofs giving consistently higher L_h temperatures than metal roofs, likely due to differences in albedo.

3.3.2 Nighttime case

At 00:30 (Fig. 10b), the vertical profiles of simulated L_h (Fig. 5.16) experience a similar shape for locations over the road and over lawns with a local maxima in the range $1 < z/z_b < 2$. Near-surface positions above lawns remain the lowest L_h of all profiles. Modelled L_h increases immediately and rapidly with height above the two lawn positions as warmer night-time walls come into the FOV of the radiometers. For both positions over lawns, L_h decreases with height above z/z_b = 1.5 as roofs come to dominate the FOV. It is however interesting to note the variation between the profiles above the east and west lawns. Above the eastern lawn the profile of L_h decreases more slowly with height. This is likely a remnant from afternoon heating delivering irradiance to warm the west-facing walls of the eastern row of houses for longer in the evening. Cooling of house facades and lawns on the western side of the canyon has a head start, so L_h over western lawn positions decrease faster. Even with this difference, by $z/z_b = 6.3$, the RMSE between all positions converge near 387 $\mathrm{W\,m^{-2}}$. There is no significant variation in the observed profiles over lawns at the different horizontal slices.

Above roads and lanes, the profiles show that L_h is increasing until z/z_b = 1.0 and then decreasing. There is no significant variation in the observed profiles over roads and lanes at the three different along-canyon cross-sections.

Above-roofs, L_h shows substantial variation depending on position along the canyon due to different daytime heating (albedo) and thermal admittance (roof isolation). In general however the magnitude of the variation is less than during the daytime: temperature differences between different roofs are lower. Profiles of L_h above western houses show an increase with height until convergence with all other profiles at z/z_b = 6.3.

3.4 Impact on radiometer placement

All simulated pyrgeometer positions from all modelled time steps show convergence of L_h with height. The overall RMSE value between the 18 different locations at each time step and height is shown in Table 4. It is assumed the 18 positions cover a large enough sample of horizontal variability. To measure a consistent L_h regardless of location with a typical positional error of < 1, < 5 and $< 10\,\mathrm{W\,m^{-2}}$ a hemispherical pyrgeometer would have to be placed at $z/z_b > 7.5$, > 4.0 and > 2.4, respectively, during daytime. At night, the curves fall < 1, < 5 and $< 10\,\mathrm{W\,m^{-2}}$ at $z/z_b > 6.3$, > 3.2 and > 1.9, respectively. The RMSE between the different horizontal positions as a function of height is well approximated by an exponential formulation:

Table 4. RMSE of selected horizontal positions for increase in radiometer altitude. Road positions are not included.

z (m)	z/z_b	RMSE 13:30 ($\mathrm{W\,m^{-2}}$)	RMSE 18:30 ($\mathrm{W\,m^{-2}}$)	RMSE 00:30 ($\mathrm{W\,m^{-2}}$)	RMSE 06:30 ($\mathrm{W\,m^{-2}}$)
8	1.28	20.2	14.9	11.2	9.2
12	1.93	14.9	9.3	11.1	10.8
16	2.57	9.6	6.5	8.5	8.4
20	3.21	6.2	3.8	5.8	5.7
24	3.85	4.4	2.6	3.8	3.8
28	4.49	3.4	1.8	2.5	2.5
32	5.14	2.8	1.5	1.6	1.7
36	5.78	2.3	1.1	1.1	1.2
40	6.42	1.8	0.83	0.78	0.86
44	7.06	1.4	0.56	0.62	0.68
48	7.70	1.1	0.46	0.44	0.52
52	8.35	0.85	0.36	0.34	0.41
58	9.31	0.53	0.32	0.28	0.34

$$\mathrm{RMSE} = a \exp(-b\, z/z_b), \tag{7}$$

where b is a coefficient that describes the rate of convergence relative to mean building height, and a is a coefficient that describes the hypothetical RMSE at ground level ($z/z_b = 0$) in $\mathrm{W\,m^{-2}}$. In the current case, b seems invariant with time for all four time steps simulated at $b = 0.475$ ($R^2 = 0.991$). Practically, a is roughly proportional to the RMSE of the subfacet L_uparrow of the complete urban surface and is highest during daytime ($\approx 30\,\mathrm{W\,m^{-2}}$) and lower in the evening and morning transition periods ($\approx 20\,\mathrm{W\,m^{-2}}$).

In terms of horizontal location, convergence occurs more rapidly above locations that are either road or lawns; a radiometer positioned at z/z_b = 5 would record a flux within $1.5\,\mathrm{W\,m^{-2}}$ of the convergent value. This means pyrgeometers are more representative for the neighbourhood average in this area when installed over the canyon compared to over roofs, explained by the energy balance and geometric structure of these two extremes. The preferred location to create the most representative sample at lower heights would be halfway between the canyon/lanes and roofs.

The differences between horizontal positions shown here are much larger than Roberts (2010) found using a scale model of a idealized urban canopy in a hardware scale model. This indicates that the large variation present in upwelling longwave radiation with horizontal location is also driven by facet-scale variability on material and geometry, as the scale model of Roberts (2010) had low material variation and a repetitive geometry. Voogt (2008) demonstrates the importance of microscale temperature variability due to varying material properties on the effective anisotropy of an urban canopy. The regular geometry and uniform material of an idealized urban surface in a controlled scale experiment may miss a significant fraction of the effective anisotropy. A simulation done by Hénon et al. (2011) using the SOLENE model for a realistic urban fragment in Marseille with increased detail found larger differences (up to 20 % of the value of L_h) between horizontal locations at z/z_b = 1.5 but they found that differences in L_h were insignificant at z/z_b = 2.5. This is a lower height than that calculated here, and may be due to the greater building density of Marseille compared to the open-set Vancouver Sunset morphology, as well as wider material differences of the facets in the current study (no extensive lawns in Marseille). Increased building density reduces the view factor of walls and the lack of lawns changes the thermal properties of the ground.

3.5 Hemispherical radiometric temperature

In some applications it is helpful to express measured L_h as a hemispherical radiometric temperature $T_{0,\mathrm{h}}$ (Norman and Becker, 1995). $T_{0,\mathrm{h}}$ was calculated in absence of emissivity effects inverting the Stefan–Boltzmann law $(T_{0,h}/\sigma)^{0.25}$ (i.e. using $\varepsilon = 1.0$). Then $T_{0,\mathrm{h}}$ was compared to $T_{0,\mathrm{C}}$ and $T_{0,\mathrm{d}}(\phi = 0)$ for a nadir view in the four time steps examined (with $T_{0,\mathrm{h}}$ being averaged at $z/z_b = 8$ over all 18 profiles). Surprisingly, the directional radiometric surface temperature in the nadir, $T_{0,\mathrm{d}}(\phi = 0)$, appears to be a better estimator for $T_{0,\mathrm{C}}$ than $T_{0,\mathrm{h}}$. The RMSE for $T_{0,\mathrm{d}}(\phi = 0)$–$T_{0,\mathrm{C}}$ over the 24 h cycle is computed as 1.4 K, while the RMSE for $T_{0,\mathrm{h}}$–$T_{0,\mathrm{C}}$ is higher at 1.8 K.

4 Summary and conclusions

A methodology was developed and successfully applied to simulate the measurement bias of different remote sensors when inferring longwave emittance and surface temperatures of a convoluted, three dimensional urban surface. Unlike previous observational studies, mostly based on helicopter or aircraft measurements (e.g. Lagouarde et al., 2004; Sugawara and Takamura, 2006), the current methodology allows a high repetition in time and a spatial resolution at the sub-facet scale.

The bias of various FOVs (nadir, hemispherical, oblique) was quantified. The methodology was based on a panoramic time sequential thermography data set (PTST) recorded over a 24 h cycle using a thermal camera on a hydraulic mast in an urban street canyon. Methods from micrometeorology, computer vision and computer graphics were combined to project the PTST onto a detailed, photogrammetrically derived 3-D model of the urban structure surrounding the hydraulic mast, then corrected for atmospheric and emissivity effects to retrieve T_0 at sub-facet scale. Facets of the 3-D model that were not seen by the thermal camera were statistically gap-filled with data from other areas based on selected predictors (ψ_sky, material, orientation of facet). The resulting three dimensional model allowed the computation of the complete surface temperature $T_{0,\mathrm{C}}$ and the simulation of the directional and hemispherical radiometric surface temperatures in absence of emissivity effects at varying locations and orientations in and above the canyon.

Simulated directional radiometric surface temperatures for the various sensors showed that none were properly able to record the true complete surface temperature, and all experienced biases. Deviations between −1.9 K (day) and +1.6 K (night) were found between the directional radiative surface temperature in the nadir, $T_{0,\mathrm{d}}(\phi = 0)$, and $T_{0,\mathrm{C}}$. For simulated off-nadir view directions, the deviation between $T_{0,\mathrm{d}}(\phi, \Omega)$ and $T_{0,\mathrm{C}}$ was larger; ranging from −2.6 to +2.9 K. The effective thermal anisotropy of the surface was highest in the daytime (particularly at sunrise and sunset, up to 3.5 K) which is consistent with the literature. The effective thermal anisotropy in this study was similar in form but lower in magnitude to that measured over a residential area in Vancouver in Voogt and Oke (1998) (near 8 K in their study). The same pattern of a east–west effective thermal anisotropy following the street canyon orientation was reproduced in the current study.

The results are valid for a suburban surface without tall vegetation. In this regard, the selected study canyon is quite unusual. Dyce (2014) modelled a larger subset of the same neighbourhood including the canyon section investigated here (called Vancouver-Sunset "NW Subdomain" in Dyce (2014)). His model incorporates the effects of tall vegetation. Modelled estimates of anisotropy suggest the tree-free effective anisotropy to be 2.1 K (12:00 LMST) and 2.4 K (09:00 LMST). However when trees are added the effective anisotropy increased to 4.7 and 2.8 K, respectively.

The hemispherical sensor simulations showed that the proper placement of a hemispherical downward-facing pyrgeometer above a city is critical to measure an outgoing longwave radiation flux density $L_\uparrow$ that is representative for the entire urban canopy. The average horizontal positional error for a sensor at 2, 3 and 5 times the mean building height z_b was 11.2, 6.3 and 2.0 $\mathrm{W\,m^{-2}}$. The positional error between different horizontal locations in retrieving $L_\uparrow$ decreased exponentially with height. Generally above 3.5 z_b the horizontal positional error was less than the typical accuracy of high-quality pyrgeometers (±5 $\mathrm{W\,m^{-2}}$).

The approach taken in the paper could easily be extended to other urban morphometries, geographic locations and different wavebands (e.g. albedo). The equipment needed is relatively simple – a scanning (spectral) imaging system and a detailed USM. To increase the coverage, several systems on multiple towers or ground locations could reduce the need for gap filling. Also, the gap-filling algorithm could be improved by incorporating the effects of facet shading and shading history, which are both currently not considered as selection criteria in the search for similar cases to fill gaps.

It might be possible to develop empirical correction factors to allow estimation of $T_{0,\mathrm{C}}$ from $T_{0,\mathrm{d}}$. However, it is likely that these factors would be unique to a particular geometry and might only be applicable in the neighbourhood/city that they were created in.

An interesting theoretical question that remains is the choice of the appropriate bulk-surface temperature of an urban canopy in one-dimensional urban surface parameterizations. While the energy balance of the UCL is greatly controlled by $T_{0,\mathrm{f}}$ of the canyon walls and floor, the roof temperature may be less important to most of the UCL. Many multilayer urban surface parameterization specifically model $T_{0,\mathrm{f}}$ of individual facets (walls, ground, roof) (Grimmond et al., 2010). But the surface temperature "seen" from a layer in the atmosphere above the city is also not simply described by adding the roofs to get the complete surface temperature $T_{0,\mathrm{C}}$, but rather the hemispherical radiometric temperature $T_{0,\mathrm{h}}$. This work also showed that $T_{0,\mathrm{C}} \neq T_{0,\mathrm{h}}$ because the relative weighting (view factors) are different for a hemispherical sensor compared to the pure area weighting of the complete urban surface.

The Supplement related to this article is available online at doi:10.5194/amt-8-2699-2015-supplement.

Acknowledgements. This study was supported by the Canadian Foundation for Climate and Atmospheric Sciences (CFCAS) as part of the Network Grant "Environmental Prediction in Canadian Cities" (EPiCC) and by NSERC Discovery Grants (A. Christen, J. A. Voogt). Selected equipment was provided by Environment Canada. Fred Meier (Technische Universität Berlin) provided MODTRAN runs for atmospheric corrections in the specific context. Nicholas Coops (UBC Forestry) and his research group provided processed LiDaR surface data and Bob Woodham (UBC Computer Science) provided technical assistance. F. Chagnon, B. Crawford, A. Jones, R. Ketler, K. Liss, T. Oke, C. Siemens, and D. van der Kamp helped with the planning, infrastructure and/or field work of PTST data acquisition. We thank E. Leinberger for drawing figures.

Edited by: H. Worden

References

Adderley, C. D.: The effect of preferential view direction on measured urban surface temperature, Master's thesis, University of British Columbia, 2012.

Arya, S. P.: Introduction to Micrometeorology, Academic Press, 2 Edn., 2008.

Christen, A. and Vogt, R.: Energy and radiation balance of a central European city, Int. J. Climatol., 24, 1395–1421, 2004.

Christen, A., Meier, F., and Scherer, D.: High-frequency fluctuations of surface temperatures in an urban environment, Theor. Appl. Climatol., 108, 301–324, 2012.

Christen, A., Oke, T. R., Steyn, D. G., and Roth, M.: 35 years of urban climate research at the "Vancouver-Sunset" flux tower, FluxLetter, 5, 29–36, 2013.

Chudnovsky, A., Ben-Dor, E., and Saaroni, H.: Diurnal thermal behavior of selected urban objects using remote sensing measurements, Energy Build., 36, 1063–1074, 2004.

Cleugh, H. A. and Oke, T. R.: Suburban-rural energy balance comparisons in summer for Vancouver, Bound.-Lay. Meteorol., 36, 351–369, 1986.

Dyce, D. R.: A sensor view model to investigate the influence of tree crowns on effective urban thermal anisotropy, Master's thesis, The University of Western Ontario, London, ON, 2014.

Flir Systems: ThermoVision A40M Operator's Manual, 2004.

Goodwin, N. R., Coops, N. C., Tooke, T. R., Christen, A., and Voogt, J. A.: Characterizing urban surface cover and structure with airborne lidar technology, Can. J. Remote Sens., 35, 297–309, 2009.

Grimmond, C. S. B., Blackett, M., Best, M., Barlow, J., Baik, J., Belcher, S. E., Bohnenstengel, S. I., Calmet, I., Chen, F., Dandou, A., Fortuniak, K., Gouvea, M. L., Hamdi, R., Hendry, M., Kawai, T., Kawamoto, Y., Kondo, H., Krayenhoff, E. S., Lee, S. H., Loridan, T., Martilli, A., Masson, V., Miao, S., Oleson, K., Pigeon, G., Porson, A., Ryu, Y. H., Salamanca, F., Shashua-Bar, L., Steeneveld, G. J., Tombrou, M., Voogt, J. A., Young, D. T., and Zhang, N.: The international urban energy balance models comparison project: first results from phase 1, J. Appl. Meteorol. Climatol., 49, 1268–1292, 2010.

Harman, I., Best, M., and Belcher, S. E.: Radiative exchange in an urban street canyon, Bound.-Lay. Meteorol., 110, 301–316, 2004.

Hénon, A., Mestayer, P. G., Groleau, D., and Voogt, J.: High resolution thermo-radiative modeling of an urban fragment in Marseilles city center during the UBL-ESCOMPTE campaign, Building Environ., 46, 1747–1764, 2011.

Johnson, G. T. and Watson, I. D.: The determination of view-factors in urban canyons, J. Climate Appl. Meteorol., 23, 329–335, 1984.

Kotthaus, S., Smith, T. E. L., Wooster, M. J., and Grimmond, C. S. B.: Derivation of an urban materials spectral library through emittance and reflectance spectroscopy, ISPRS J. Photogramm., 94, 194–212, 2014.

Krayenhoff, E. S., Christen, A., Martilli, A., and Oke, T. R.: A multi-layer radiation model for urban neighbourhoods with trees, Bound.-Lay. Meteorol., 151, 139–178, 2014.

Lagouarde, J., Moreau, P., Irvine, M., Bonnefond, J., Voogt, J. A., and Solliec, F.: Airborne experimental measurements of the angular variations in surface temperature over urban areas: case study of Marseille (France), Remote Sens. Environ., 93, 443–462, 2004.

Lagouarde, J. P., Henon, A., Kurz, B., Moreau, P., Irvine, M., Voogt, J., and Mestayer, P.: Modelling daytime thermal infrared directional anisotropy over Toulouse city centre, Remote Sens. Environ., 114, 87–105, 2010.

Masson, V., Grimmond, C. S. B., and Oke, T. R.: Evaluation of the Town Energy Balance (TEB) scheme with direct measurements from dry districts in two cities, J. Appl. Meteorol., 41, 1011–1026, 2002.

Meier, F., Scherer, D., Richters, J., and Christen, A.: Atmospheric correction of thermal-infrared imagery of the 3-D urban environment acquired in oblique viewing geometry, Atmos. Meas. Tech., 4, 909–922, doi:10.5194/amt-4-909-2011, 2011.

Nikiforiadis, F. and Pitts, A.: 3D digital geometric reconstruction of the urban environment for daylight simulation studies, in: Eighth International Building Simulation Conference, Eindhoven, 2003.

Norman, J. M. and Becker, F.: Terminology in thermal infrared remote-sensing of natural surfaces, Agr. Forest Meteorol., 77, 153–166, 1995.

Offerle, B. D., Grimmond, C. S. B., Fortuniak, K., and Pawlak, W.: Intraurban differences of surface energy fluxes in a central European city, J. Appl. Meteorol., 45, 125–136, 2006.

Oke, T. R.: Canyon geometry and the nocturnal urban heat island: Comparison of scale model and field observations, Int. J. Climatol., 1, 237–254, 1981.

Oke, T. R.: The energetic basis of the urban heat-island, Q. J. Roy. Meteorol. Soc., 108, 1–24, 1982.

Oke, T. R.: Boundary Layer Climates, 1987.

Roberts, S. M.: Three-dimensional radiation flux source areas in urban areas, Ph.D. thesis, University of British Columbia, 2010.

Salmond, J. A., Roth, M., Oke, T. R., Christen, A., and Voogt, J. A.: Can surface-cover tiles be summed to give neighborhood fluxes in cities?, J. Appl. Meteorol. Climatol., 51, 133–149, 2012.

Shirley, P., Ashikhmin, M., and Marschner, S.: Fundamentals of Computer Graphics, 2009.

Stewart, I. D. and Oke, T. R.: Local climate zones for urban temperature studies, B. Am. Meteorol. Soc., 93, 1879–1900, 2012.

Sugawara, H. and Takamura, T.: Longwave radiation flux from an urban canopy: Evaluation via measurements of directional radiometric temperature, Remote Sensing of Environment, 104, 226–237, 2006.

Voogt, J. A.: Assessment of an urban sensor view model for thermal anisotropy, Remote Sens. Environ., 112, 482–495, 2008.

Voogt, J. A. and Oke, T. R.: Complete urban surface temperatures, J. Appl. Meteorol., 1997.

Voogt, J. A. and Oke, T. R.: Radiometric temperatures of urban canyon walls obtained from vehicle traverses, Theor. Appl. Climatol., 60, 199–217, 1998.

Voogt, J. A. and Oke, T. R.: Thermal remote sensing of urban climates, Remote Sens. Environ., 86, 370–384, 2003.